Electronic Supplementary Information

Transition-Metal Interdiffusion and Solid Electrolyte Poisoning in All-Solid-State Batteries Revealed by Cryo-TEM

Ruizhuo Zhang,[a] Florian Strauss,*[a] Lin Jiang,[b] Lee Casalena,[b] Letian Li,[c] Jürgen Janek,[ad] Aleksandr Kondrakov[ae] and Torsten Brezesinski*[a]

[a] Battery and Electrochemistry Laboratory (BELLA), Institute of Nanotechnology, Karlsruhe Institute of Technology, Hermann-von-Helmholtz-Platz 1, 76344 Eggenstein-Leopoldshafen, Germany.

[b] Thermo Fisher Scientific, 5350 NE Dawson Creek Drive, Hillsboro, OR 97124, USA.

[c] Thermo Fisher Scientific, Achtseweg Noord 5, 5651 GG Eindhoven, Netherlands.

[d] Institute of Physical Chemistry and Center for Materials Research, Justus-Liebig-University Giessen, Heinrich-Buff-Ring 17, 35392 Giessen, Germany.

[e] BASF SE, 67056 Ludwigshafen, Germany.

*Email: florian.strauss@kit.edu, torsten.brezesinski@kit.edu

Materials and Cell Preparation

The pristine cathode active material, $LiNi_{0.85}Co_{0.1}Mn_{0.05}O_2$ (BASF SE), was first annealed at 750 °C for 3 h under O_2 flow to remove the residual Li (carbonate species) present on the surface (with 5 °C/min heating and cooling rates). Both Li_6PS_5Cl solid electrolyte (NEI Corp.) showing a room-temperature ionic conductivity of around 2 mS/cm and Oppanol binder (polyisobutylene, BASF SE) were used as received. The carbon additive, Super C65 (TIMCAL Ltd.), and carbon-coated $Li_4Ti_5O_{12}$ (NEI Corp.) were dried at 300 °C in a dynamic vacuum overnight prior to use. The preparation procedure of the slurry-cast cathode and cell assembly are described in detail elsewhere.[1,2]

Electrochemical Testing

After a 1 h OCV rest period, electrochemical testing was done at different rates of 0.1C, 0.2C, 0.5C, 1.0C and 2.0C for two cycles each (with 1C = 190 mA/g). The subsequent 150 cycles were performed at a 1.0C rate. The voltage range was set to 1.35-2.75 V vs $Li_4Ti_5O_{12}/Li_7Ti_5O_{12}$ (i.e., around 2.9-4.3V vs Li^+/Li). Galvanostatic cycling was done with the help of a MACCOR battery cycler at 45 °C and 81 MPa external pressure. Two identical cells were cycled to ensure data consistency and reliability.

Cryo-STEM and EELS Measurements

In the current study, the Thermo Scientific IGST workflow solution was used to enable a DualBeam to TEM workflow by protecting both bulk sample and prepared lamella in Ar atmosphere with a CleanConnect™ transfer module. Using the CleanConnect™ module, cathode foils from the SSB cells were successfully transferred from the glovebox to a Helios 5 Hydra DualBeam without signs of surface oxidation. Due to the beam and temperature sensitivity of the solid electrolyte and the cathode electrolyte interphase in the cycled electrodes, the entire TEM lamella preparation process, including bulk milling, lift out, attach to the TEM grid and final thinning, was carried out at cryogenic temperature (−178 °C) with a Thermo Scientific cryo-stage and cryo-EasyLift nano-manipulator. To achieve minimal ion damage to the final lamella, all ion-milling processes were carried out with Ar plasma-focused ion beam from a Helios 5 Hydra multi-ion species plasma FIB. To minimize surface amorphization on the prepared lamella, the final thinned region was polished with 5 kV and then subsequently 2 kV Ar beam. The prepared lamella was then transferred back to the glovebox under Ar-gas protection using the CleanConnect™ transfer module. Inside the glovebox, the lamella was loaded to a MelBuild double tilt LN2 Atmos Defend Holder, which allows lamella transfer from the glovebox to a TEM under Ar-gas protection.

An illustration of the workflow process is shown in Fig. S2. After loading the bulk sample (cathode) into the microscope with the inert gas-transfer module, a 2 μm thick Pt layer was deposited by FIB to protect the top surface of the sample, as well as to reduce curtaining artefacts during subsequent milling. After the protective layer deposition, the bulk sample was cooled down to cryogenic temperature (−178 °C) to avoid beam damage or heat-induced artefact formation upon milling. Once the bulk sample reached the target temperature, two large

trenches were milled with Ar-plasma FIB to form a relatively thick (40 µm × 20 µm ×10 µm) chunk ready for *in situ* lift out (Fig. S2a). To avoid sample warm-up during the lift-out process, a cryogenic lift-out needle is used. The lift-out needle was cooled to −178 °C, together with the stage, to decrease the temperature difference between needle and chunk. Also, the cryogenic needle can keep the temperature of the chunk after lifting it out from the bulk sample (Fig. S2b). Next, the chunk was transferred to a Cu TEM grid. The Cu grid is located on the bulk cryogenic stage and therefore holds a temperature of −178 °C (Fig. S2c). After welding the chunk to the Cu TEM grid with the redeposition method, the cryogenic lift-out needle is cut free from the chunk (Fig. S2d). The chunk is then thinned systematically by gradually reducing the FIB current, from its original thickness (~10 µm) all the way to electron transparency (100-200 nm). To keep sample integrity during thinning, the final region of interest was achieved by opening smaller windows on the bulk lamella (Fig. S2e). In summary, the whole TEM sample preparation, including bulk milling, chunk lift out, chunk transfer and chunk thinning, was done at cryogenic temperature to avoid beam damage or heat-induced artefacts.

S/TEM images, EDS and EELS data were acquired with a Thermo Scientific Talos F200X CFEG S/TEM at 200 kV. The temperature was actively controlled at −155 °C using the MelBuild Atmos Defend Holder with the LN2 as a cooling agent to protect the samples from beam damage during data acquisition. TEM images were captured in Velox software using a Ceta-16 M CMOS camera. STEM images with different image contrasts were acquired in Velox software simultaneously using HAADF, DF and BF detectors. Drift-corrected frame integration (DCFI) was utilized to counter any sample drift and to improve the signal-to-noise ratio by integrating multiple frames in both TEM and STEM modes. EDS maps and spectra were collected in STEM mode with a probe current of 100 pA using a Bruker Dual-X EDS system. EELS data were collected using a Gatan GIF Continuum 1066 system with a 5 mm entrance aperture and an energy dispersion of 0.3 eV/Ch. The energy resolution was around 0.8 eV.

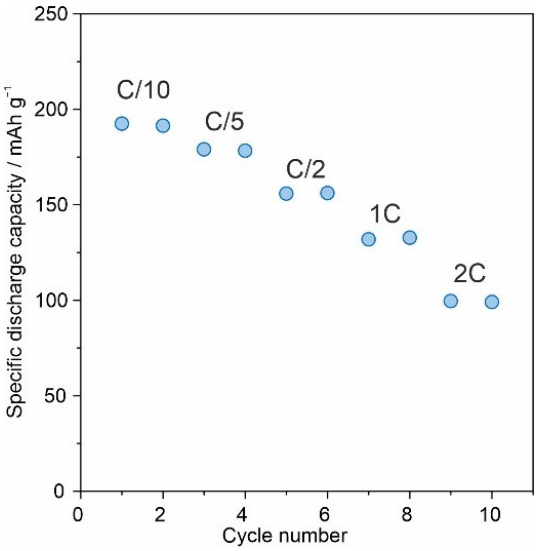

Fig. S1 Rate capability of the slurry-cast cathode in pellet-stack SSB cells at 45 °C.

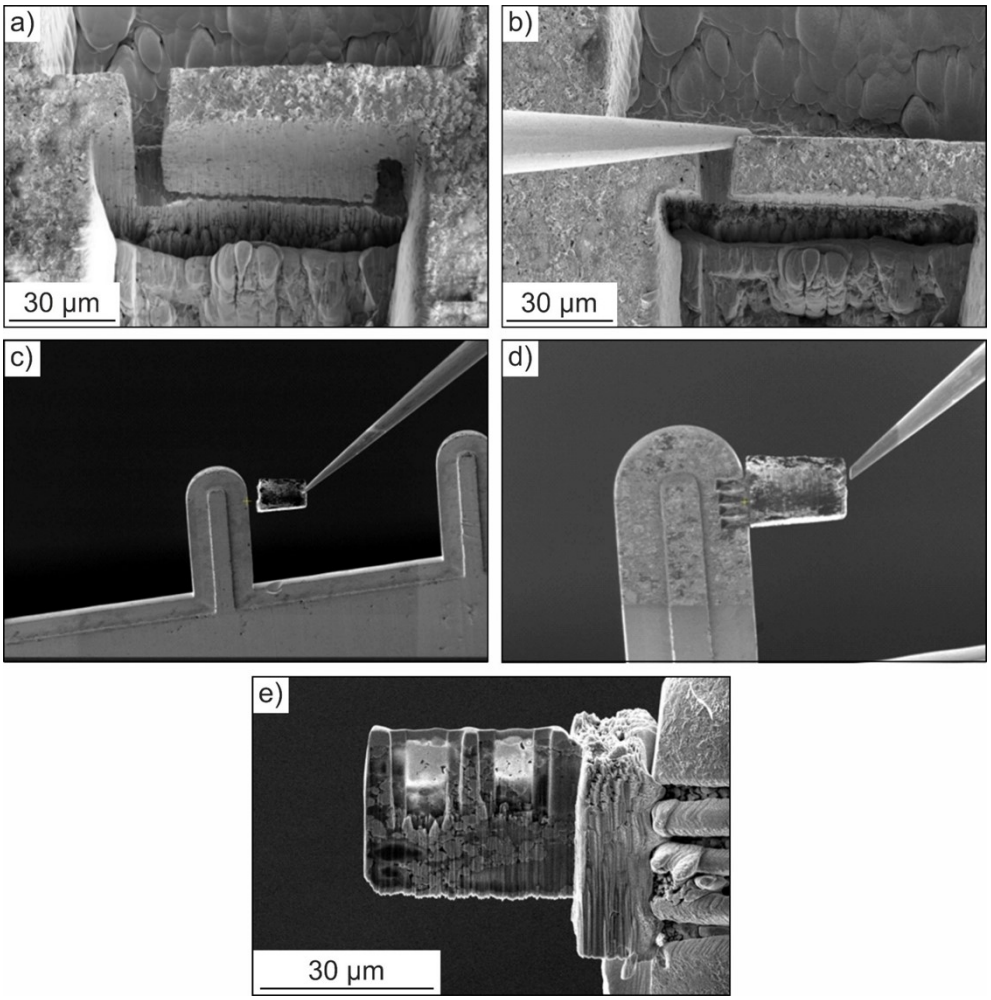

Fig. S2 Specimen preparation for TEM/EELS investigations. (a) Chunk creation and (b) lift out at cryogenic temperature using a cryogenic lift-out needle. (c) Chunk transfer to TEM grid under cryogenic temperature and (d) attachment by redeposition welding. (e) The lamella is thinned at two regions of interest (bright areas) to ensure electron transparency.

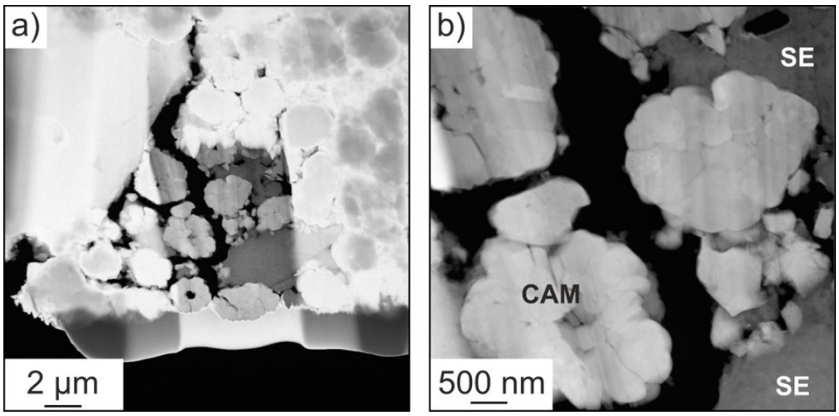

Fig. S3 (a, b) Cross-sectional cryo-STEM (HAADF) images at different magnifications of the cycled cathode. CAM and SE regions are indicated in (b).

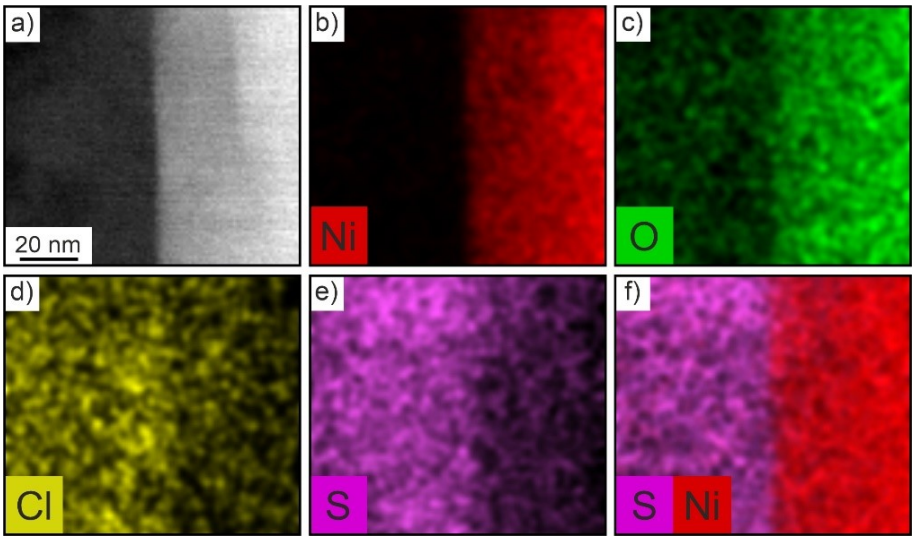

Fig. S4 (a) Cryo-STEM (HAADF) image of the pristine CAM/SE interface and (b-e) corresponding EDS maps for Ni, O, Cl and S. (f) S and Ni overlap map indicating a well-defined and "clean" interface.

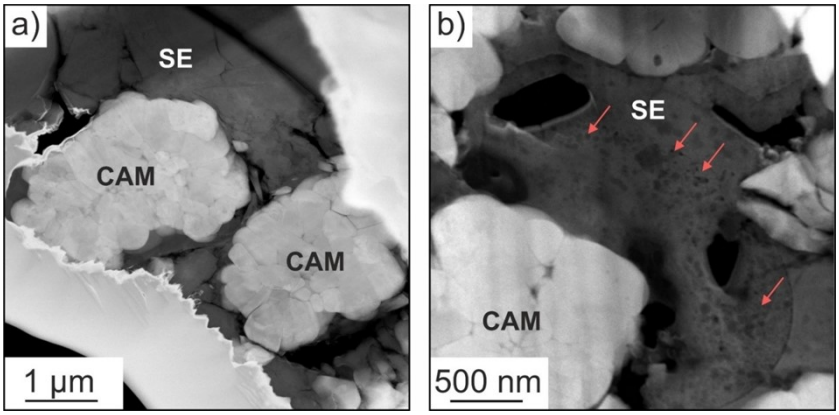

Fig. S5 Cross-sectional cryo-STEM (HAADF) images of (a) pristine and (b) cycled cathode. The formation of darker contrast spots in the SE region is indicated by arrows in (b).

EELS Ionization Edge Treatment and L_3/L_2 Ratio Analysis

Edge Treatment

Background subtraction was done with Digital-Micrograph GMS 3 software using the power-law fit method. A linear least square fit was applied to the log-log transform over an energy region preceding the ionization threshold of the experimental spectrum. The power-law profile was fitted in the pre-edge region and extrapolated to the post-edge region. The core-loss intensities were extracted by subtraction of the background intensity from the acquired signal. Low-pass numerical filtering was used to smooth the spectra.

L_3/L_2 Analysis

The white line ratio of the transition metals was calculated based on the integrated area of L_3 and L_2. The continuum background was fitted by a straight line within the threshold regions. A

step function with height ratio of 2:1 for L_3 and L_2 was applied to account for the multiplicity of the 2p states. The area ratio between L_3 and L_2, which was integrated between white line and fitted background, was used to analyze the valence state.

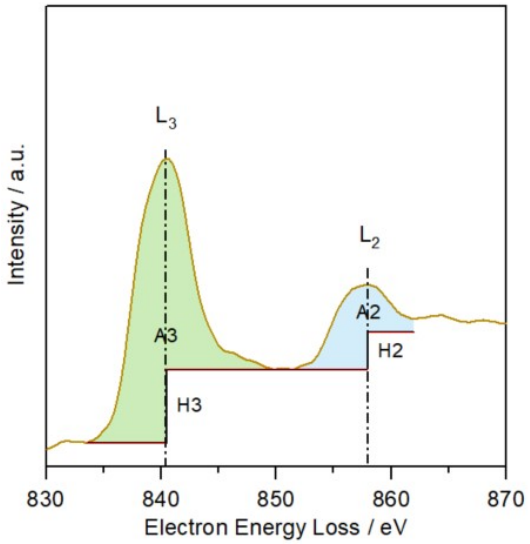

Fig. S6 Example for the calculation of the integrated area ratio between L_3 and L_2 in the high-loss region of transition metals. A linear step function with height H3:H2 = 2:1 is fitted to the continuum background within the threshold region. The L_3/L_2 ratio analysis is based on the integrated area ratio of A3(L_3) to A2(L_2).

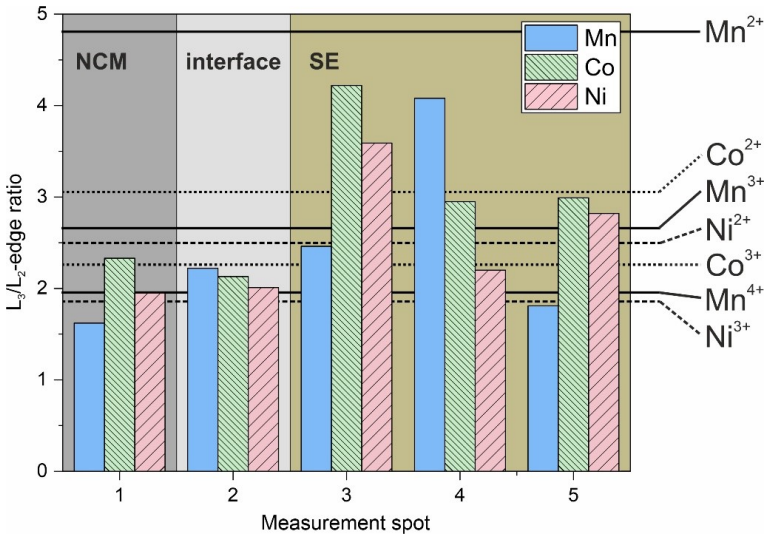

Fig. S7 L_3/L_2-edge ratios for Ni, Co and Mn from EELS analysis of different areas (P1 to P5, see Figs. 3 and 4 in the main text). Specific values are provided in Tab. S1 and different L_3/L_2-ratios associated with different oxidation states (from literature) are denoted by solid and dashed lines.[3–8]

Tab. S1 Summary of EELS results for O, Ni, Co and Mn. Δ*E* represents the difference in energy loss between O K-edge and pre-edge. Note that for P3 and P4, no O K pre-edge feature was observed.

Spot	Δ*E* / eV	Ni L_3/L_2	Co L_3/L_2	Mn L_3/L_2
P1	12.0	1.95	2.33	1.62
P2	10.8	2.01	2.13	2.22
P3	-	3.59	4.22	2.46
P4	-	2.20	2.95	4.08
P5	8.7	2.82	2.99	1.81

References

1 J. H. Teo, F. Strauss, Đ. Tripković, S. Schweidler, Y. Ma, M. Bianchini, J. Janek and T. Brezesinski, *Cell Reports Physical Science*, 2021, **2**, 100465.

2 J. H. Teo, F. Strauss, F. Walther, Y. Ma, S. Payandeh, T. Scherer, M. Bianchini, J. Janek and T. Brezesinski, *Mater. Futures*, 2022, **1**, 015102.

3 N. Twu, M. Metzger, M. Balasubramanian, C. Marino, X. Li, H. Chen, H. Gasteiger and G. Ceder, *Chem. Mater.*, 2017, **29**, 2584.

4 D. Mohanty, A. S. Sefat, J. Li, R. A. Meisner, A. J. Rondinone, E. A. Payzant, D. P. Abraham, D. L. Wood III and C. Daniel, *Phys. Chem. Chem. Phys.*, 2013, **15**, 19496.

5 C. R. Fell, D. Qian, K. J. Carroll, M. Chi, J. L. Jones and Y. S. Meng, *Chem. Mater.*, 2013, **25**, 1621.

6 T. G. Sparrow, B. G. Williams, C. N. R. Rao and J.-M. Thomas, *Chem. Phys. Lett.,* 1984, **108**, 547.

7 B. Serment, C. Brochon, G. Hadziioannou, S. Buffière, A. Demourgues and M. Gaudon, *RSC Adv.*, 2019, **9**, 34125.

8 C. Ma, J. Alvarado, J. Xu, R. J. Clément, M. Kodur, W. Tong, C. P. Grey and Y. S. Meng, *J. Am. Chem. Soc.*, 2017, **139**, 4835.